A Comparative Study on the Beam and Continuum Finite Element Models for the Rail-wheel Vibration

Q. Xie[1], Y.X. Zhou[2, 3], Y. Zhan[4], K.Y. Sze[4], W.S. Han[1]

[1]*School of Highway, Chang'an University, Xi'an, Shaanxi, P.R. China*
[2]*Faculty of Civil Engineering and Mechanics, Jiangsu University, Zhenjiang, Jiangsu, P.R.China*
[3]*Faculty of Science, Harbin Institute of Technology, Shenzhen, Guangdong, P.R.China*
[4]*Department of Mechanical Engineering, The University of Hong Kong, Pokfulam, Hong Kong SAR, P.R. China*

Published in **Inter. J. of Structural Stability and Dynamics** Vol. 19, No. 7 (2019) 1950076 (28 pages) DOI: 10.1142/S0219455419500767

Received 2 August 2018, Accepted 12 March 2019, Published 5 April 2019

Abstract

The rail-wheel interaction can induce train and track vibrations and consequently lead to noise impact, passengers' discomfort, high maintenance cost, etc. Due to the complexity of the rail-wheel interaction and the high cost of field tests, as well as the difficulties in data collection, numerical analyses have been widely resorted to for predicting the train and track vibrations, for which numerous numerical models have been developed. According to track modeling approaches, the numerical models can be generally divided into two categories, i.e., beam models and continuum finite element (FE) models. In this paper, these two models are systematically compared and discussed. First, a typical beam model of Wu and Thompson (2004) is introduced, based on which a modified model is then established. Second, a plane continuum FE model with high mesh quality is established, in which the transition mesh generation, contact treatment and element size determination are presented. Numerical tests are conducted to validate the proposed plane FE model. Finally, both the beam and the plane continuum FE models are examined through typical rail-wheel interaction examples, in which the linear response of the track as well as the rail-wheel vibrations under both a single rolling wheel and two rolling wheels are analyzed. The results show that most of the vibration trends obtained from the two models agree well with each other. Nevertheless, it is noteworthy that the continuum FE model has superiorities, especially for analyzing vibrations at higher frequencies. The present study can be of considerable help for designers and engineers in the railway industry to achieve the trade-off between the simulation demands and the computational cost.

Keywords

Rail-wheel vibration, finite element, beam model, continuum model, transition mesh

1. Introduction

Railway transportation, which is an efficient way to relieve road transportation pressure, has developed rapidly in recent years for both intercity and urban passenger transport. When the train is running, both the train and the track vibrate, which can lead to noise impact, passengers' discomfort, high maintenance cost, etc. Various theories and methods have been developed to investigate and predict the vibrations of the train and the track, among which numerical simulations have proven to be an effective and efficient tool, with many numerical models having been established in the literature.[1, 2] According to the track modeling approaches, these numerical models can be generally divided into two categories: beam models and continuum finite element (FE) models.[3, 4]

Due to their simplicity and efficiency, beam models are widely used to predict rail vibrations. The Euler-Bernoulli beam (EB) model, which neglects shear deformation, was employed in the early years. In 1976, Remington et al.[5] developed an EB model to predict the rolling noise due to the rail-wheel interaction, in which the rail was approximated as a beam lying upon a continuous elastic foundation. Later, the effects of discrete supports provided by sleepers were taken into consideration in the EB models by researchers such as Munhal et al.[6] and Grassie et al.[7] Wu and Yang[8-10] developed several train-rail-bridge interaction models, where the rail is modeled as an EB model to simulate the vehicle and bridge responses as well as the rail-wheel contact forces. Based on EB theory, the vibration of the train under braking conditions and the vibration of the track considering rail weld irregularities were also examined.[11, 12] On the other hand, the Timoshenko beam (TB) model, which considers shear deformation, has also been well-received in rail-wheel simulations for its superior accuracy compared to that of the EB model. In 1982, a TB model in which both the rail and sleepers were modeled as flexible beams was developed by Clark et al.[13] to study the vertical rail vibration caused by the rail corrugation. Ilias[14] proposed a discretely supported TB model to investigate the influences of the rail pad stiffness on the rail-wheel interaction forces and the growth of the rail corrugation. Hosseinkhani et al.[15] modeled the track using a TB model on a viscoelastic foundation to simulate the dynamic deflection alongside the railways. Wu and Thompson[16-21] conducted systematic studies on the rail-wheel vibration using TB models, where additional features, such as the effect of multiple wheels, wheel flats and rail joints, rail corrugation, etc., were incorporated. To explore the interspersed track vibration induced by a moving train, a TB rail-wheel interaction model was developed by Kaewunruen et al.[22]

With advances in computing technology, continuum FE models have been increasingly employed to simulate the rail-wheel vibration with a refined approximation. These models can be divided into four categories according to the modeling objectives, i.e., stress analysis, rolling contact fatigue (RCF), wear analysis and thermal contact analysis.

i. Stress analyses, which are essential for understanding and further predicting rail/wheel fatigue and failure behaviors, are conducted via continuum FE models because the stress distribution cannot be generally reflected by the beam model. For instance, Sladkowski et al.[23] proposed a three dimensional (3D) FE model to explore the effects of the rail and wheel profiles on the contact stress distribution; Sun et al.[24] developed an elastic 3D FE model to study the dynamic behavior of a rail under a wheel passing through a curved track; a 3D FE model was built by Wen et al.[25] to investigate the effects of the height difference defect, train speed and axle load

on the contact stress at the railhead; and a 2D rail-wheel FE model was proposed by Chen et al.[26] to explore the effects of insulated rail joints on the contact stress.

ii. The RCF prediction, which is an extensively focused topic in the railway industry, has also been implemented using continuum FE models. For example, Kabo et al.[27] proposed a two-dimensional (2D) FE model to explore how the material defect size affected the RCF of railway wheels; Bogdanski et al.[28] developed a 2D multi-size FE model to predict the RCF crack; and Ringsberg[29] performed an elastic-plastic FE analysis that cooperated with the strain-life method to predict the lifetime of RCF.

iii. The mechanism of wear can also be explained using a continuum FE analysis. For instance, Daves et al.[30] developed a 2D FE model to investigate the effect of surface roughness on the sliding-rolling wear; Chang et al.[31] studied the evolution of the rail/wheel profile due to wear via 3D FE dynamic analyses; and other researchers, such as Chen et al.[32], Wen et al.[33], Andersson et al.[34] and Naeimi et al.[35], investigated the mechanisms behind the occurrence of corrugation using continuum FE models.

iv. The effect of thermal contact, which may cause severe heat damage at the rail/wheel surfaces, has also been simulated using continuum FE analyses. For example, Wu et al.[36] developed a 2D frictional FE model to discuss the effect of rail-wheel thermal contact on the residual deformation/stress and found that the contact stresses were observably increased when considering the thermal effect; Ramanan et al.[37] proposed a 3D rail-wheel FE model to study the thermal stresses due to braking; a 2D FE simulation was conducted by M. Petereson[38] to discuss the transient thermal convection-diffusion during block braking; and Sun et al.[39] employed 3D FE models to investigate the impact of frictional heat caused by the relative sliding between the rail and the wheel on the contact stress and temperature field.

Although both beam and continuum FE models are widely employed in rail-wheel simulations, a systematic comparison between them, to the authors' best knowledge, is still absent.[40] Generally, for static analyses or dynamic analyses over small time periods, continuum FE models are preferred. In contrast, beam models are usually selected for dynamic analyses over relatively large time periods. What triggered this comparative study was wanting to ascertain whether these common understandings are pertinent or not. In the present study, one typical beam FE model and one plane continuum FE model are developed, and then the dynamic behaviors of the rail-wheel vibration simulated using each model are systematically compared and discussed. The paper is organized as follows: a modified beam FE model based on Wu and Thompson's work is proposed in Section 2; a plane continuum FE model is proposed and validated through numerical tests in Section 3; typical FE simulations on rail/wheel vibrations are conducted using the two models and their results are compared and discussed in Section 4; and a conclusion is given in Section 5. It is expected that the main features of the two models revealed in this paper can provide a more comprehensive understanding of the numerical simulation of rail-wheel vibrations, which will be helpful when choosing between different models.

2. Beam FE Model

In this section Wu and Thompson's typical beam model[41] is briefly introduced, based on which a modified beam FE model is then developed. In Wu and Thompson's model, the rail is modeled as a conventional TB and the discrete supports, including sleepers, rail-pads and the ballast, are simplified

as discrete mass-spring systems, see Fig. 1. The wheel is treated as a lumped mass, M_w, while the vehicle weight is simplified as a dead weight, W, loading on the wheel mass. The track receptance subjected to a harmonic force in the frequency domain at n (e.g., n=12) equal-spaced positions within a sleeper span is first calculated. Then, the track model is transformed from the frequency domain to the time domain using mathematical treatments. Finally, the response of the wheel is connected to the rail by a nonlinear Hertzian contact spring, in which the rail-wheel interaction force is defined as:

$$f_c = \begin{cases} C_H (x_w - x_r)^{3/2}, x_w - x_r > 0 \\ 0, x_w - x_r \le 0 \end{cases} \quad (1)$$

where C_H is the Hertzian constant and x_r and x_w are the vertical displacements of the rail and the wheel at the contact position, respectively. Noteworthy that the Hertzian constant C_H is determined according to the Hertzian contact theory, which assumes small strain and non-adhesive and frictionless contact conditions.[42]

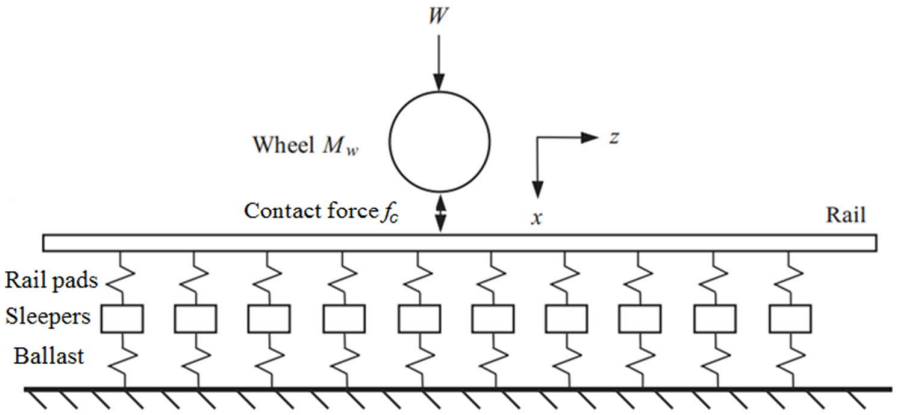

Fig. 1 Timoshenko beam model of the rail-wheel dynamic interaction by Wu and Thompson.[41]

Although Wu and Thompson's beam model has been successfully applied to various engineering problems[21, 41], modifications are made here to further improve its accuracy. The modified beam FE model is illustrated in Fig. 2. First, the wheel/track vibrations are excited by moving interaction forces instead of non-moving harmonic forces, considering that the wheel is moving along the rail throughout. Consequently, the error caused by the relative speed of the structural waves in the track and train can be reduced, e.g., the error of the rail acceleration is decreased by approximately 3~5% in general cases.[42] Second, the modified beam model is solved using an explicit time integration method, thus it can be directly applied in the time domain and extended to nonlinear analyses. Third, a rail section covering 69 sleeper spans rather than only one single span is selected, considering that it should be sufficiently long to capture the approaching and leaving effects of the train on the track vibration and reduce the influence of the longitudinal boundary conditions.[42]

The modified beam FE model is established in Abaqus. Two-node TB elements are applied to discretize the rail. The element size determination will be discussed in Section 2.1. For the discrete support consisting of rail-pads, sleepers and the ballast, the sleepers are simplified as lumped masses,

and the rail-pads and the ballast are both modeled using a linear spring element and a dashpot element, as shown in Fig. 2. Additionally, the primary suspension of the vehicle is taken into account and modeled by a set of elastic springs and dampers in order to improve the model accuracy. The parameters related to the track and vehicle are extracted from the website of Hong Kong Mass Transit Railway Corporation Limited (HK MTR)[43] and are provided in Table 1, unless otherwise specified.

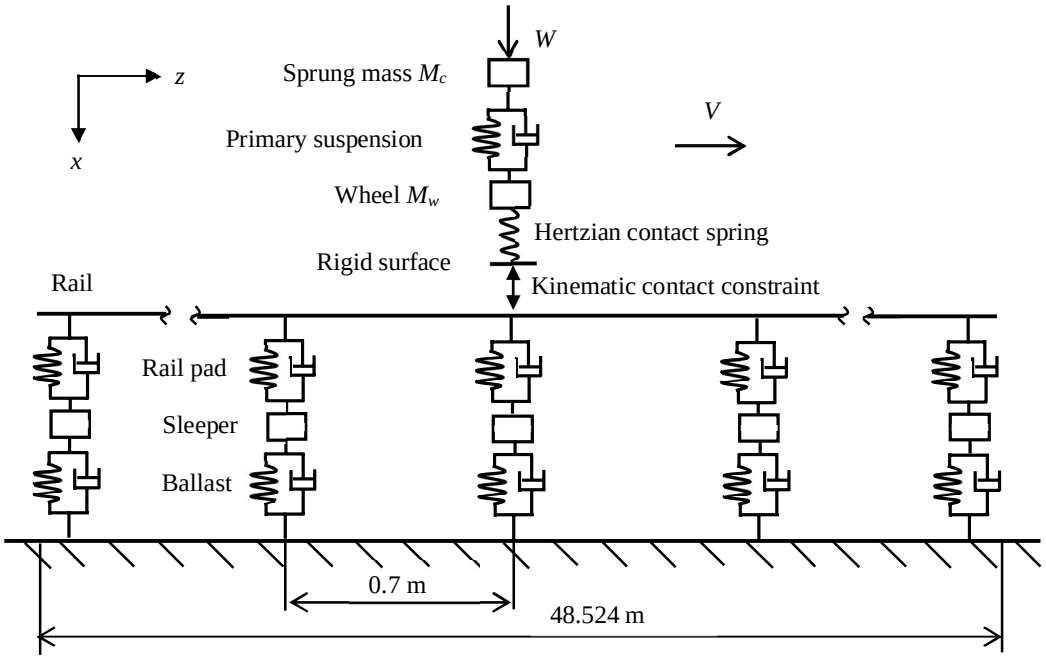

Fig. 2 Modified beam FE model for the rail-wheel dynamic interaction.

In the modified beam FE model, a nonlinear spring element is applied to build the force-displacement relationship of the rail-wheel interaction, i.e., the nonlinear Hertzian relationship in Wu and Thompson's work,[41] see Eq. (1). Since the Hertzian constant depends highly on the shape of the contact area[42], which is difficult to measure accurately, it is simply taken as the value given in Wu and Thompson's model.[41] To ensure the spring node, which denotes the contact point on the rail that is always sliding on the rail surface, a rigid surface is introduced to be sliding on the rail, see Fig. 2. The characteristic length of the rigid surface as well as the mass should be sufficiently small to reduce the effects of this artificial surface. Here the characteristic length is assumed to be only slightly larger than the beam element size in the potential contact zone and thus the rigid surface cannot penetrate the rail, while the mass is empirically chosen to be one-tenth of the mass of the adjacent rail node. It deserves mentioning that numerical tests have been conducted and the results reveal that, as long as the characteristic length does not exceed thrice that of the element size, a rather limited difference can be found. The kinematic contact algorithm in Abaqus/Explicit is chosen to build the contact condition between the rigid surface and the rail surface. Because neither ballast springs nor rail-pad springs can bear the shear force along the longitudinal direction, the longitudinal displacements of the sleepers are constrained. This simplification is reasonable because in reality each sleeper is

embedded in the ballast and its longitudinal motion can be neglected. The above modified beam FE model will be employed in subsequent simulations and denoted as the "beam FE model" in the results.

Table 1. Vehicle and track parameters used in the beam FE model.

Components	Parameters	Values
Vehicle body [44]	Sprung mass M_c (kg)	10000
Wheel mass	M_w (kg)	561
Primary suspension [45]	Spring stiffness (kN/m)	665
	Dashpot coefficient (kN·s/m)	15
Sleeper mass	M_s (kg)	150
Sleeper span	d (m)	0.7
Rail-pad	Spring stiffness (MN/m)	200
	Dashpot coefficient (kN·s/m)	48
Ballast	Spring stiffness (MN/m)	40
	Dashpot coefficient (kN·s/m)	43
Rail (UIC60)	Elastic modulus (GPa)	210
	Shear modulus (GPa)	80.769
	Poisson's ratio	0.3
	Density (kg/m^3)	7850
Rail cross-section	Area (m^2)	7.823×10^{-3}
	Moment of inertia about the n_1 axis (m^4)	3.155×10^{-5}
	Moment of inertia about the n_2 axis (m^4)	5.247×10^{-6}
Rail-wheel interaction[41]	Hertzian constant (GN/m$^{3/2}$)	93.7

2.1 Element Size of the Rail

A typical simulation of a single wheel rolling on a rail is performed in the present study to determine a reasonable element size for the rail. The wheel is located directly above a sleeper at t = 0. The evolution of the wheel speed versus time is shown in Fig. 3, where the wheel speed is uniformly accelerated to V = 21 m/s at t_1 = 0.2 s and then rolls at that uniform speed until t_2 = 0.3 s. The three mesh schemes given in Table 2 are considered, in which the element size of the rail is selected as 8.75, 4.375 and 0.875 mm, respectively. The vertical displacement at the wheel center during the uniform rolling period, t_1 to t_2, is predicted and plotted in Fig. 4. The two meshes with smaller element sizes, i.e., 0.875 mm and 4.375 mm, provide very similar results, thus the element size of the rail is determined to be 4.375 mm in the present modified beam FE model.

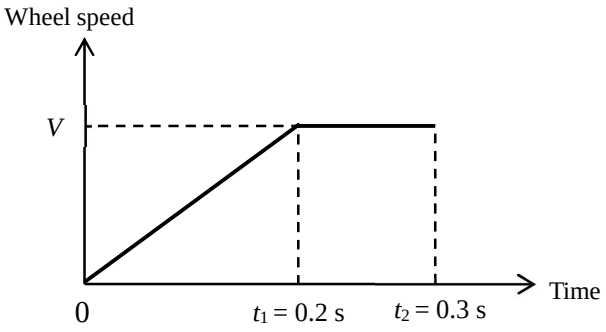

Fig. 3 Evolution of the wheel speed versus time

Table 2. Three mesh schemes of the rail

Mesh	Element Size of the Rail	Total Number of Elements in the Rail
Mesh 1	0.875	55440
Mesh 2	4.375	11828
Mesh 3	8.75	5544

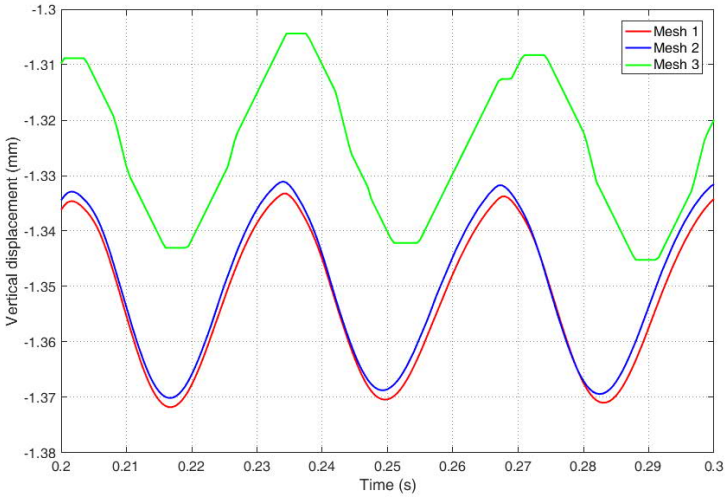

Fig. 4 Vertical displacement at the wheel center using the three rail meshes.

2.2 Validation of the Modified Beam FE Model

A simple example considering a single wheel rolling on a straight rail is studied using Wu and Thompson's beam model and the present modified beam FE model. The rail-wheel contact force and the dynamic displacement at the wheel center are predicted and compared in Fig. 5. The results obtained from the two beam models agree well with one another, except for some minor fluctuations in the contact force.

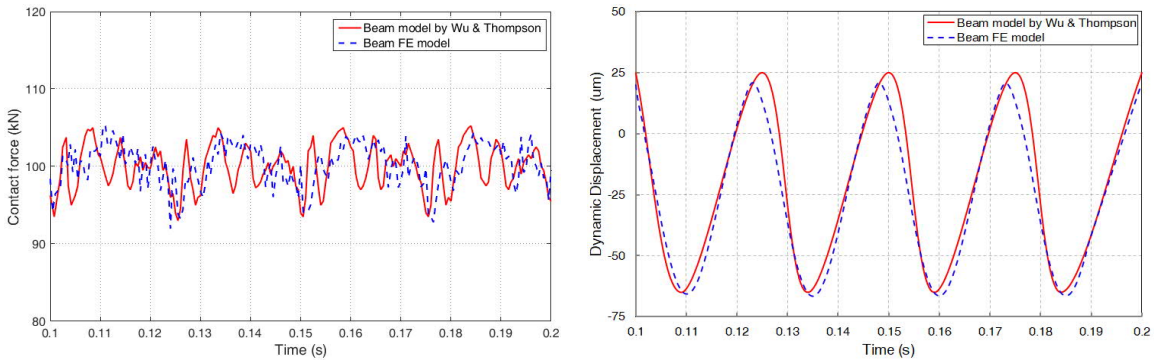

(a) (b)

Fig. 5 Time-histories of (a) the contact force and (b) the dynamic displacement at the wheel center predicted by the two beam models.

3. Plane FE Model

Plane continuum FE models are often employed in dynamic analyses because fewer elements and nodes are involved compared to their 3D counterparts and thus considerable computational costs can be saved.[38, 46] In this section, a plane continuum FE model in the Lagrangian frame is developed and implemented in Abaqus for a dynamic rail-wheel interaction. Before introducing the model in detail, it deserves mentioning that the main challenge in constructing the continuum FE model of the rail-wheel interaction system is a dilemma between the demanding of an acceptable accuracy, which requires both a high mesh quality and a small time step, and the limitation of the computational costs.

The plane continuum FE model of the rail-wheel system is composed of the track and the vehicle. The former includes the rail, rail-pads, sleepers and the ballast while the latter consists of the vehicle body, primary suspension, axles and wheelsets. The four-node quadrilateral (Q4) element is selected to model the rail and the wheel. The actual profile of the standard UIC60 rail shown in Fig. 6a is simplified as a ladder-shaped cross-section and is modeled using Q4 elements with different thicknesses assigned, as shown in Fig. 6b. The rail has the same length as in the beam FE model and a high mesh density is required within and around the contact region. If the entire rail and the wheel are both meshed with a high density, the computational cost will be dramatically increased, which makes performing the simulation unrealistic. To solve this issue, two approaches are applied here. First, the entire rail is divided into three parts, as shown in Fig. 7a. The wheel is assumed to only roll over the mid-part and the element size in the potential contact zone should be sufficiently small for contact treatments. The determination of the smallest element size in the contact zone will be discussed in Section 3.2. For the other two parts (i.e., the left-side and right-side parts) the element size can be relatively enlarged. The meshes of the three parts are 'tied' together at the interfaces where no relative movements are allowed, see Fig. 7b. Note that the meshes of the three parts are generated during the preprocessing stage and remain unchanged during the dynamic analysis to avoid oscillations and numerical noises as well as an additional computational cost brought by adaptive remeshing. Second, a transition mesh scheme (Scheme 3 in Fig. 8c) is introduced, which is selected from the three transition mesh schemes in Fig. 8 (the selection details will be presented in Section

3.1). In the discretization of the mid-part, a transition mesh layer is applied between every three mesh layers in vertical direction with a total of five transition mesh layers included. For a better approximation, the sleepers and rail-pads are both modeled using Q4 elements instead of the mass-spring system used in the beam model. The top and bottom surfaces of the rail-pads are tied with the rail and sleeper, respectively. The ballast, which is relatively far from the contact zone, is modeled using parallel linear springs and dashpots. The established track model is shown in Fig. 9.

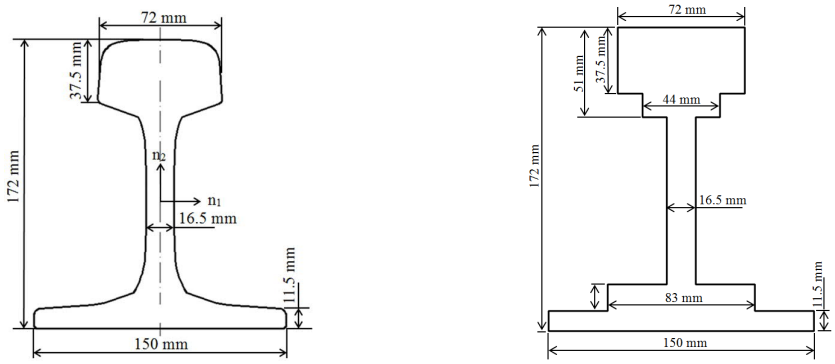

(a) (b)

Fig. 6 (a) Actual cross-section of the UIC60 rail; (b) simplified cross-sections of the rail.

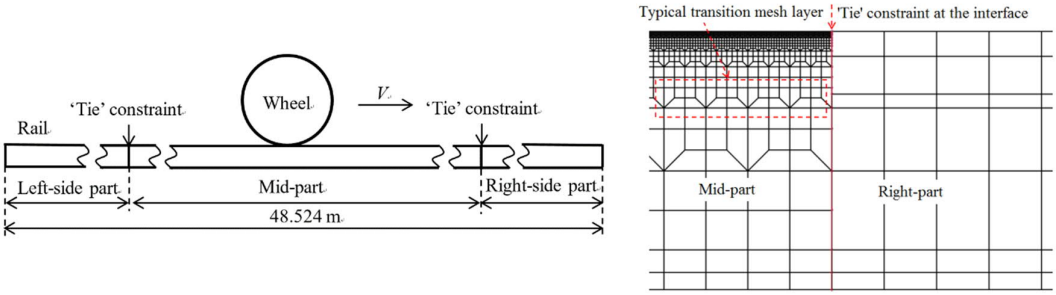

(a) (b)

Fig. 7 (a) Three parts of the rail with different mesh qualities; (b) zoom-in meshes at the transition region between the mid- and right-parts of the rail.

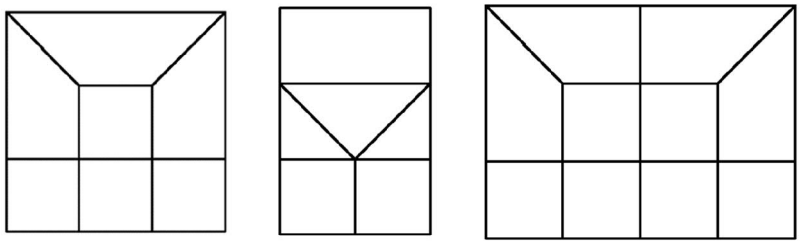

(a) (b) (c)

Fig. 8 Transition mesh schemes: (a) Scheme 1; (b) Scheme 2; (c) Scheme 3.

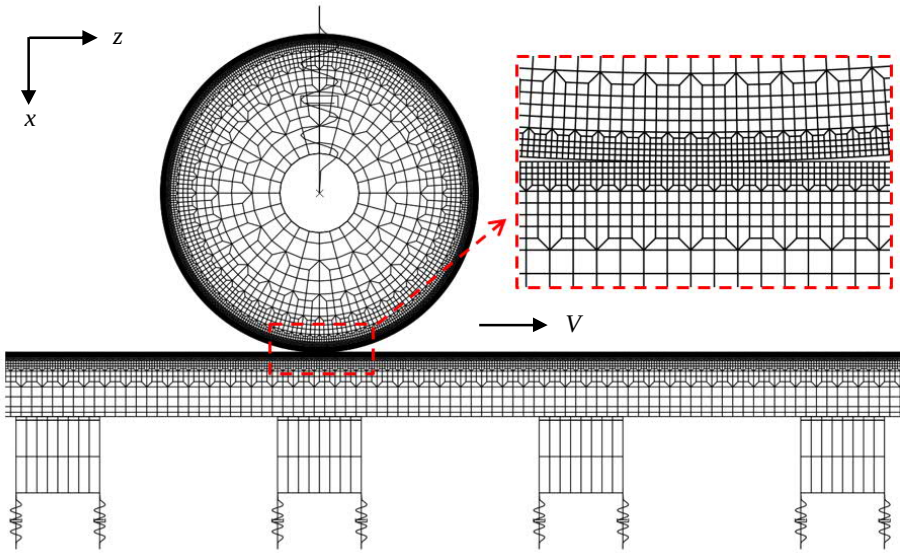

Fig. 9 A plane continuum FE model of the rail-wheel system (the smallest element size at rail-wheel interface is 0.875 × 0.875 mm).

For practical applications, the conventional wheelset consists of two wheels in the lateral direction and is mounted on a common axel.[47] Because the wheel is assumed to be rolling over a straight rail in all cases in this paper and only vertical vibration is focused on, a single wheel with half of the axle is modeled here due to symmetry. The actual profile of the SP1900 wheel is simplified as a ladder-shaped cross-section modeled by Q4 elements with different thicknesses, which is similar to the treatment on the rail. Both the smallest element size and the transition mesh scheme in the rail model are applied to model the wheel. Similarly, for the wheel mesh a transition mesh layer is employed every three mesh layers near the rail-wheel contact surface with a total of six transition mesh layers applied. The vehicle body is simplified as a lumped mass, the primary suspension is modeled using a set of linear spring and dashpot, and the vehicle weight is treated as a dead force acting on the sprung mass of the vehicle body, which is the same as that in the beam FE model. A rigid circular surface is employed to represent the axle, which transmits the load from the vehicle body to the wheel. The established vehicle model is also given in Fig. 9.

The normal interaction between the rail and wheel is directly modeled using the surface-to-surface contact treatment known as the kinematic contact enforcement method, which strictly enforces the non-penetration condition through a kinematic predictor/corrector contact algorithm.[48] In terms of a tangential contact, the friction is considered based on the classical isotropic Coulomb friction law.[49] Because the friction coefficient is difficult to measure, here both the static and dynamic friction coefficients are assumed to be 0.3 as recommended by the handbook,[47] while the actual friction type is determined according to the calculated contact pressure in each time increment. Furthermore, the creep effect of the rail-wheel system is not considered because the simulated rolling period is relatively short. All the materials in the model are assumed to be linearly elastic and geometrical nonlinearity is considered. The physical parameters related to the track and the vehicle in Table 1 are also used here with additional parameters supplemented in Table 3. The subsequent results obtained from the present plane continuum FE model will be denoted as the “plane FE model”.

Table 3. Additional parameters used in the plane FE model.

Components	Parameters	Values
Friction	Friction coefficient μ	0.3
Axle	Mass (kg)	270
Wheel (SP1900)	Elastic modulus (GPa)	210
	Poisson's ratio	0.3
	Density (kg/m^3)	7850
Sleeper	Depth (m)	1.25
	Elastic modulus (GPa)	43
	Poisson's ratio	0.15
	Density (kg/m^3)	2753
Rail pads	Depth (m)	0.15
	Elastic modulus (MPa)	60
	Poisson's ratio	0.5
	Density (kg/m^3)	1200

3.1 Transition Mesh Scheme

A variety of transition mesh schemes have been proposed for the mesh generation[50, 51], among which the three commonly used transition mesh schemes in 2D problems are depicted in Fig. 8. To assess their performances, a cantilever beam subjected to a vertical shear force P at its free end is considered, see Fig. 10a.[52] When the beam undergoes both bending and shearing deformation its mechanical behavior is similar to that of the track in the rail-wheel system. The beam is meshed using the three transition mesh schemes as shown in Fig. 10b-d, respectively. These meshes are designed so that they all possess six elements along the bottom surface of the beam and the total numbers of nodes are close to each other, i.e., 21, 22 and 23, respectively. The deflections at the bottom right corner are reported in Table 4. Mesh 3 in Fig. 10d yields the most accurate result, while the other two meshes give relatively rigid predictions, which is attributed to the poor mesh quality for the trapezoidal elements with a large aspect ratio in Mesh 1 and a high proportion of triangular elements in Mesh 2. Therefore, the transition mesh scheme used in Mesh 3, namely, Scheme 3 in Fig. 8c, is selected here for the mesh generation of the rail and wheel.

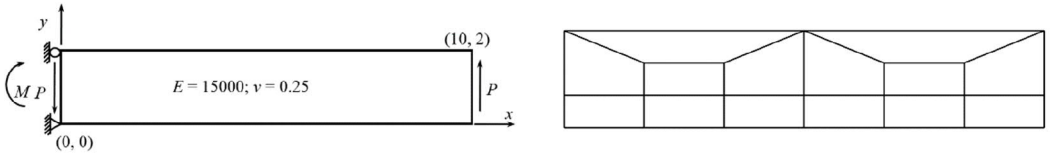

(a) (b)

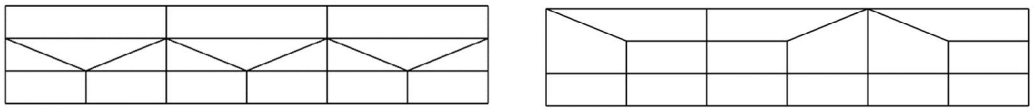

(c) (d)

Fig. 10 Cantilever beam problem. (a) Loading condition: P = 300 and M = 3000; (b) Mesh 1; (c) Mesh 2; (d) Mesh 3.

Table 4. Vertical deflection at the bottom right corner of the cantilever.

Transition mesh scheme	FE results	Analytical solution	Error (%)
Mesh 1 (14 elements)	6.32	10.23	38.2
Mesh 2 (18 elements)	8.64		15.5
Mesh 3 (15 elements)	9.50		7.1

3.2 Element Size at the Contact Zone

A convergence study is conducted here to determine a reasonable element size at the contact zone. Three mesh conditions are considered, in which the element sizes at the contact zone are selected as 1.75×1.75 mm, 0.875×0.875 mm and 0.4375×0.4375 mm, respectively. For all three meshes, the rail and wheel are discretized into five and six transition mesh layers, respectively. With all other parameters being identical, a dead force of 100 kN is loaded on the sprung mass and the resulted contact pressure on the rail is predicted and plotted in Fig. 11. The 0.875×0.875 mm and 0.4375×0.4375 mm meshes produce very similar predictions, thus the preferred element size at the contact zone is selected as 0.875 × 0.875 mm, considering the computational efficiency and the total numbers of elements in the rail and wheel being 70019 and 31392, respectively.

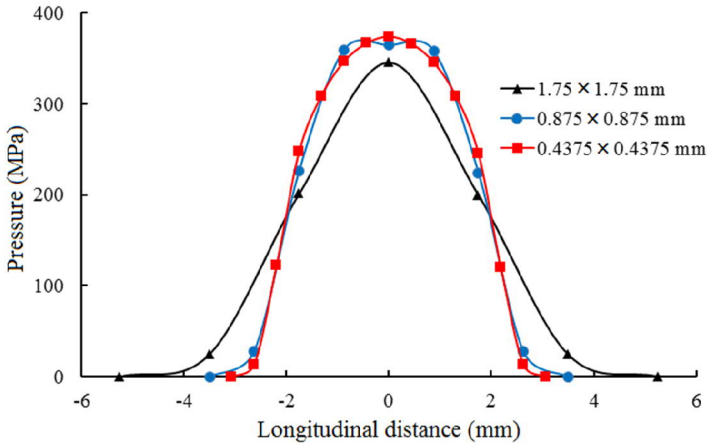

Fig. 11 Contact pressure predicted with different element sizes at the contact zone.

4. Comparative Study Based on Numerical Examples

In this section, both the modified beam FE model in Section 2 and the plane FE model in Section 3 are applied to simulate the rail-wheel interaction. Their results are then compared and discussed.

4.1 Steady-State Analysis of the Track Vibration

The linear response of the track to a harmonic excitation force loaded at the center of a sleeper span is simulated using the two models to study the track behavior, see Fig. 12. The angular frequency of the harmonic force, ω, is considered to range from 0 to 1200 Hz, which covers the normally focused frequencies in the rail-wheel vibration. Additionally, the amplitude of the harmonic force is simply assumed to be 100 kN. The acceleration of the rail at the loading point is depicted in Fig. 13, from which the following observations can be obtained:

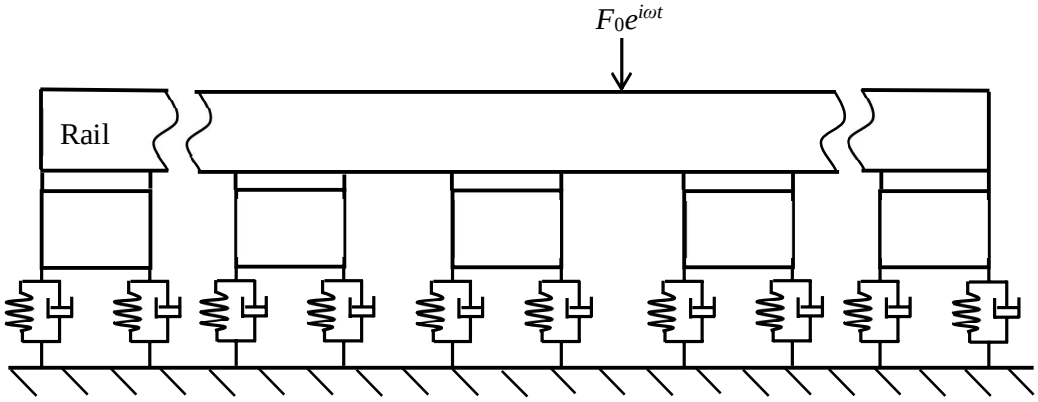

Fig. 12 Track model in a steady-state analysis

- A broad resonance peak appears at approximately 65 Hz, where the rail close to the excitation point bounces on the ballast spring in both FE models. The corresponding modes are depicted in Fig. 14.
- The second group of peaks are observed at approximately 435 Hz in the plane FE model and 340 Hz in the beam FE model, with the corresponding resonance modes plotted in Fig. 15. The difference between the two frequencies is approximately 25%, which might be attributed to the different treatments of the sleeper and the rail-pad in the two models. Recall that the sleeper is modeled as a rigid body and the rail-pad is assumed to be a linear spring element and a dashpot element with the mass neglected in the beam FE model, while both of them are treated as elastic bodies in the plane FE model.
- The pronounced peaks at approximately 855 Hz and 935 Hz are noted in the plane and beam FE models, respectively. The corresponding resonance modes plotted in Fig. 16 are induced by the periodic nature of the discrete supports[42], which are well known as the pinned-pinned vibration modes in which the rail-wheel vibration reaches its maximum at each mid-span. A similar phenomenon can also be observed in Ref. 41 and 42. The difference between the two frequencies is also caused by the different treatments on the rail-pad. Specifically, the deformation of the rail-

pad varies along the width of the sleeper in the plane FE model. However, this cannot be described by the beam FE model.

- A number of peaks are observed at frequencies ranging from 500-800 Hz and 1000 -1200 Hz in the plane FE model. Some typical vibration modes corresponding to these resonances are shown in Fig. 17 and are related to the deformation of the sleeper and rail-pad system. By contrast, the acceleration curve of the beam FE model appears relatively smooth in these two frequency regions.
- The accelerations of the two models have both positive and negative values because the acceleration is related to both the harmonic excitation force and the reaction forces produced by the deformed track and the discrete supports.

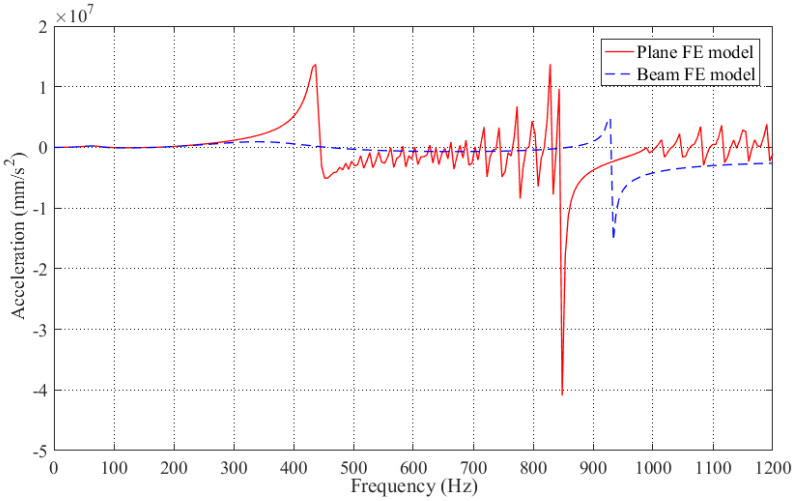

(a)

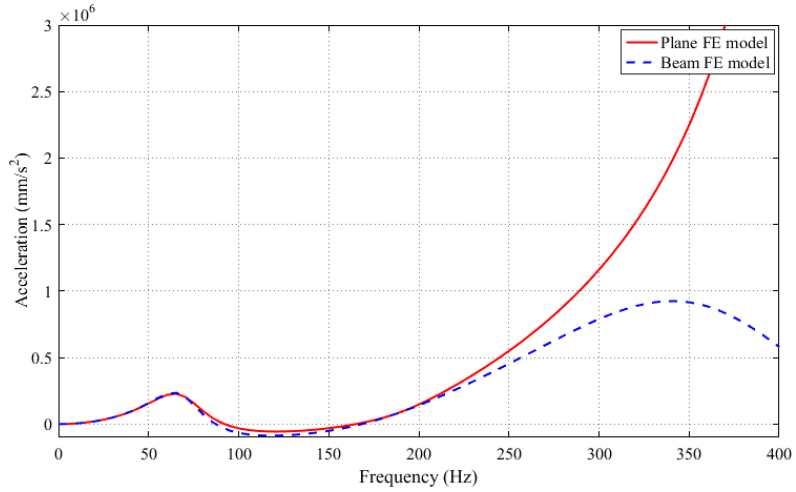

(b)

Fig. 13 Linear response of the track to a harmonic excitation force when neglecting the wheel mass: (a) the acceleration in the frequency ranging from 0 Hz to 1200 Hz; and (b) the zoom-in curve in the frequency ranging from 0 Hz to 400 Hz.

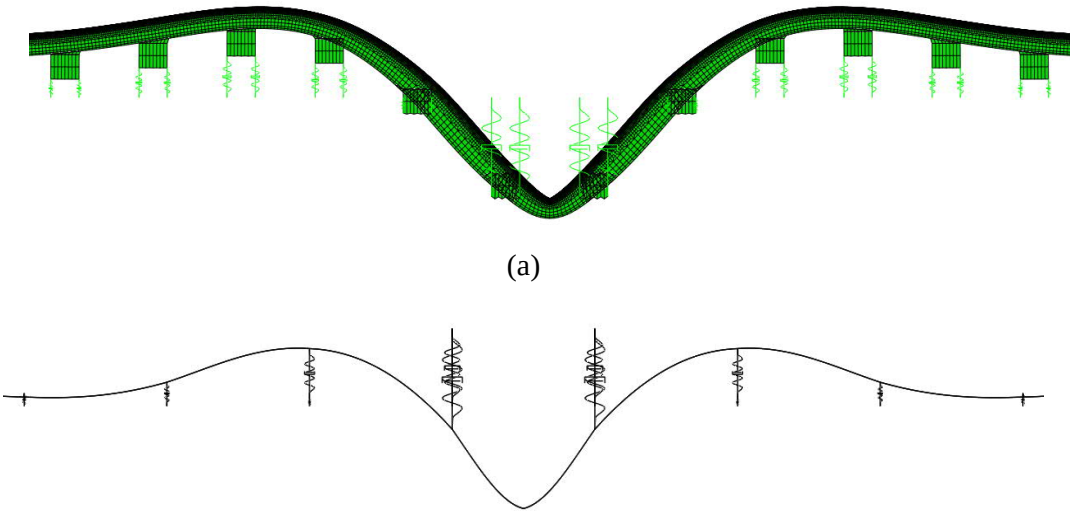

(a)

(b)

Fig. 14 Vibration modes at 65 Hz corresponding to the rail resonance on the ballast spring (scale factor: 1000) (a) Plane FE model; and (b) beam FE model.

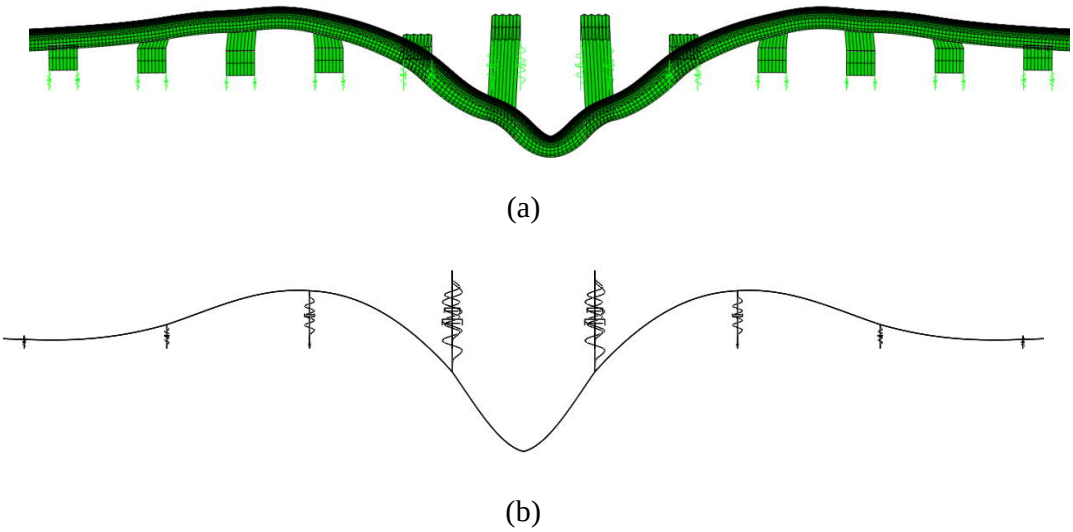

(a)

(b)

Fig. 15 Vibration modes corresponding to the rail resonance (a) at 435 Hz for the plane FE model (scale factor: 500); and (b) at 340 Hz for the beam FE model (scale factor: 3000).

Considering that the wheel is always in contact with the track and in reality possesses a mass, the linear response of track to the harmonic excitation force additionally with the wheel mass attached to the loading point is calculated using the two models. The acceleration results of the rail at the loading point are plotted in Fig. 18, from which the following observations can be obtained:

- A sharp peak and a trough are respectively observed at approximately 45 Hz and 55 Hz in both models, mainly because the rail close to the excitation point bounces on the ballast

spring but in opposite directions. The corresponding modes at the two frequencies are shown in Fig. 19 and Fig. 20, respectively.

- At approximately 225 Hz the resonances caused by the sleeper-pad system occur in both models, with the corresponding modes similar to those in Fig. 15. The pinned-pinned resonance in the plane FE model occurs at approximately 835 Hz, while it occurs at approximately 925 Hz in the beam FE model. The corresponding modes are similar to those in Fig. 16.
- Another intensive resonance arises at approximately 970 Hz in the plane FE model, with the corresponding mode depicted in Fig. 21.

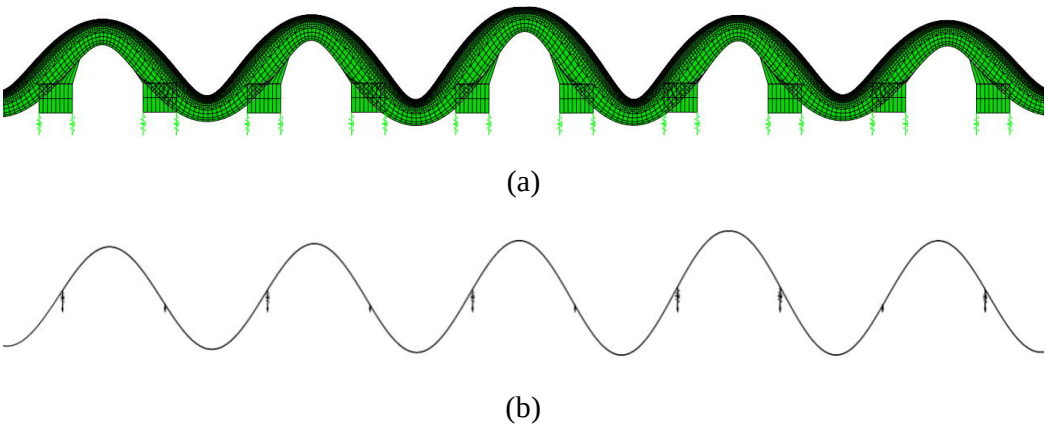

(a)

(b)

Fig. 16 Vibration modes corresponding to the rail resonance (a) at 855 Hz for the plane FE model (scale factor: 500); and (b) at 935 Hz for the beam FE model (scale factor: 1000).

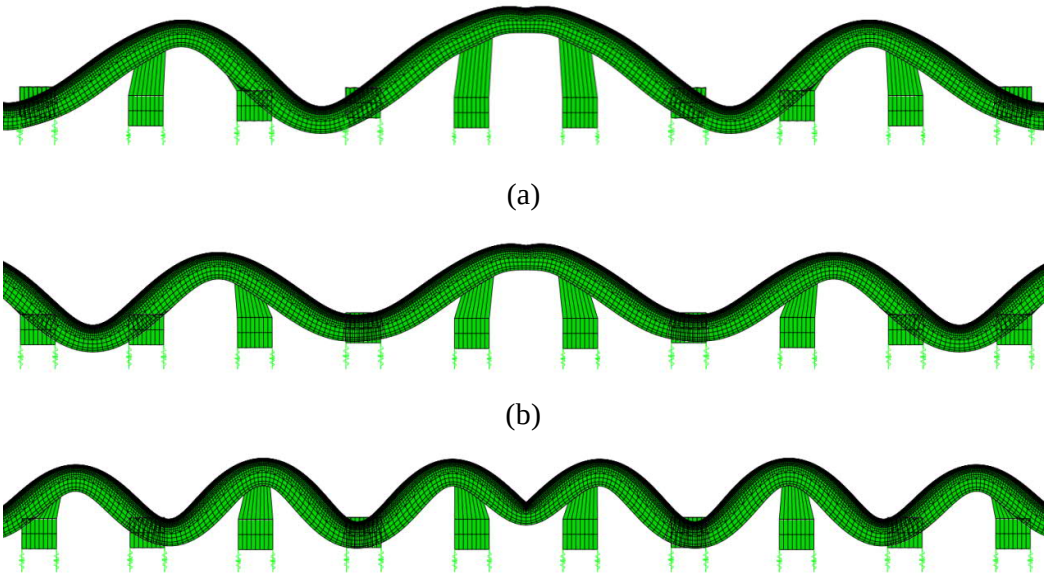

(a)

(b)

(c)

Fig. 17 Vibration modes of the plane FE model corresponding to the rail resonances in the frequency ranging 500 – 800 Hz and 1000 – 1200 Hz: (a) at 600 Hz (scale factor: 1000); (b) at 700 Hz (scale factor: 1000); and (c) at 1150 Hz (scale factor: 2000).

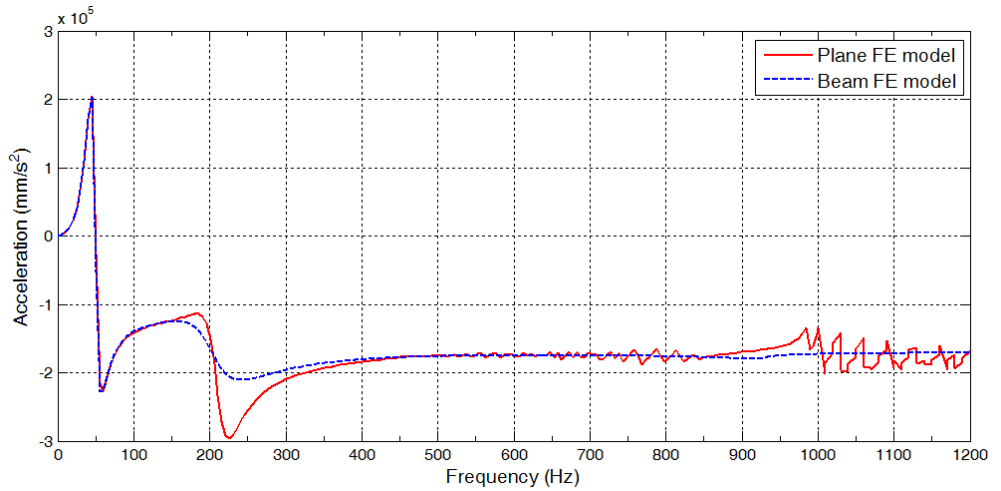

Fig. 18 Linear response of the track to a harmonic excitation force when the wheel mass is included.

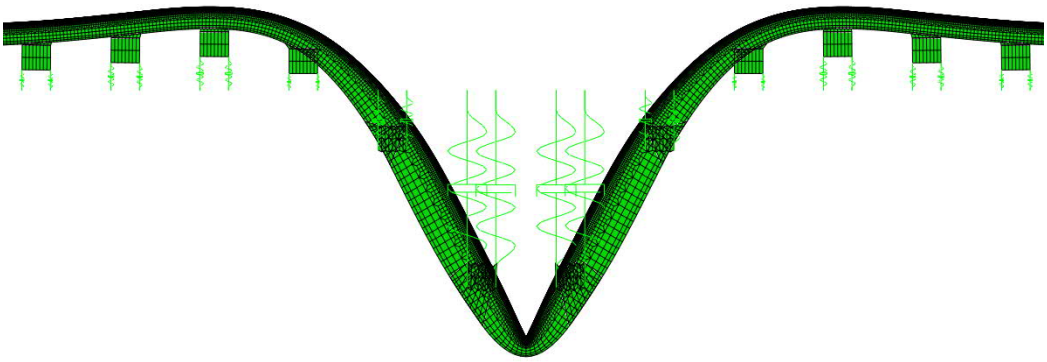

(a)

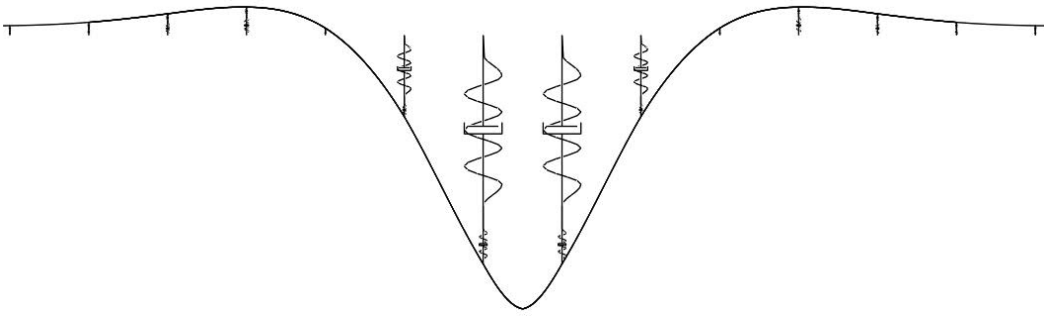

(b)

Fig. 19 Vibration modes corresponding to the rail resonance on the ballast spring at 45 Hz (scale factor: 1000). (a) Plane FE model; and (b) beam FE model.

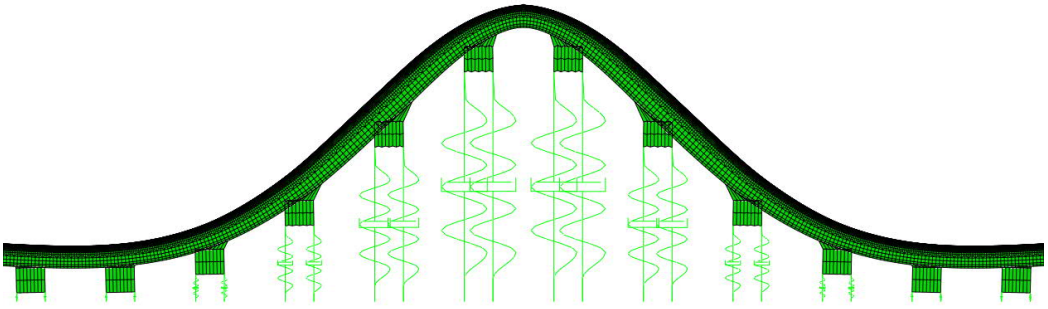

(a)

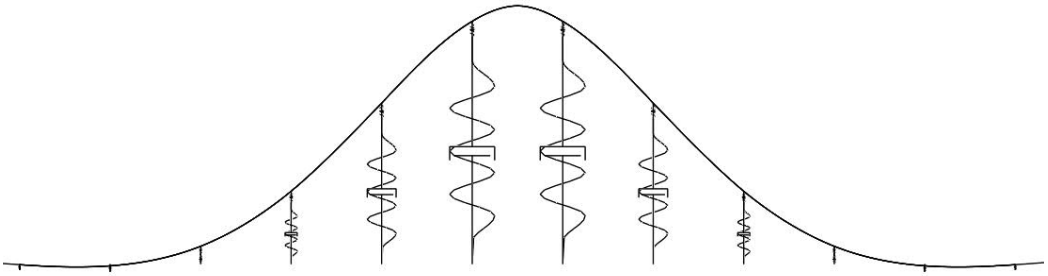

(b)

Fig. 20 Vibration modes corresponding to the rail resonance on the ballast spring at 55 Hz (scale factor: 1000). (a) Plane FE model; and (b) beam FE model.

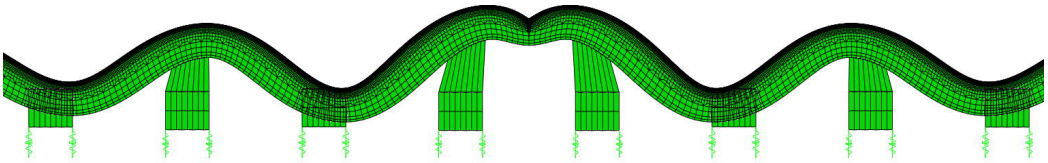

Fig. 21 Vibration mode of the plane FE model at approximately 970 Hz (scale factor: 20000).

From the above steady-state analysis of the track vibration, it is noted that the wheel mass can significantly affect the vibrational behavior of the track. When the wheel mass is included, the resonances induced by the ballast spring, the resonances caused by the sleeper-pad systems and the pinned-pinned resonance caused by the discrete supports can still be observed, but they are all shifted to lower frequencies in both models. Furthermore, although the main resonance frequencies and modes, e.g., the pinned-pinned frequency and mode, can be captured by both models, there is an observable distinction between these frequencies in the two models. Additionally, some of the resonance frequencies obtained from the plane FE model are missing in the beam FE model, which is mainly attributed to the simplified modeling of the sleepers and rail-pads.

4.2 Rail-Wheel Vibration Subjected to a Single Rolling Wheel

In this section, the rail-wheel vibration subjected to a single rolling wheel is simulated by the two models. The wheel is assumed to be rolling at (1) a regular speed of V = 21 m/s, which is close to the

running speed of HK MTR (60 - 80 km/h) and (2) a high speed of V = 42 m/s, which is twice the regular speed. The wheel is accelerated uniformly from the static status to the prescribed speed V and then runs uniformly at speed V, as described in Fig. 3. The time-histories of the rail-wheel contact force and the vertical displacement at the wheel center are predicted. The results during the uniform rolling period, i.e., t_1-t_2 in Fig. 3, are presented as follows.

For (1), a regular speed of V = 21 m/s, the rail-wheel contact forces are directly obtained in the time domain as plotted in Fig. 22a and then transformed to the frequency domain, as plotted in Fig. 22b.

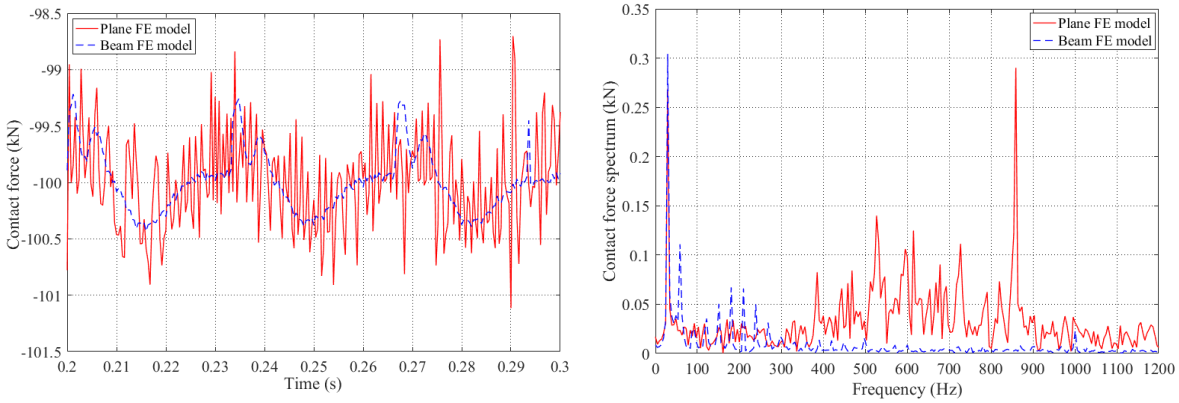

(a) (b)

Fig. 22 Contact force for rail/wheel vibration at a wheel speed of V = 21 m/s: (a) time-history of the contact force; (b) the contact force spectrum.

In Fig. 22a, the overall trends of the contact forces obtained from both models agree well and the principal frequency is identified to be the sleeper-passing frequency of 30 Hz, which is also the frequency of the first peak noted in Fig. 22b. This principal frequency can be computed by V/d, in which V is the wheel speed and d is the sleeper span. Furthermore, the difference between the contact forces is approximately 100 kN, which equals the dead force imposed on the vehicle/track system. Additionally, local strong oscillations of the contact force, which represent the rail/wheel vibration at high frequencies, can only be observed in the plane FE model. The amplitude of the force oscillation obtained from the plane FE model is almost 1.3 kN, whereas that obtained from the beam FE model is only approximately 0.6 kN.

Fig. 22b shows that the contact forces at high frequencies in the plane FE model are much greater than those in the beam FE model. A remarkable peak at approximately 860 Hz, which is close to the pinned-pinned frequency of the track, is observed in the plane FE model. However, the pinned-pinned resonance in the beam FE model is not obvious.

The time-history of the vertical displacements at the wheel center are plotted in Fig. 23. The displacements in both models appear smooth and vary periodically with the frequency, 30 Hz, which is found to be the sleeper-passing frequency. Furthermore, the displacement magnitude in the beam FE model is larger than that in the plane FE model, mainly because the Hertzian constant used in the former as well as in Wu and Thompson's model[41] is close to the lower bound according to the Hertzian

contact theory.[42] By contrast, the dynamic rail-wheel interaction in the plane FE model is realized through a direct contact treatment on the wheel and rail, which are assumed to be 2D elastic deformable continuums.

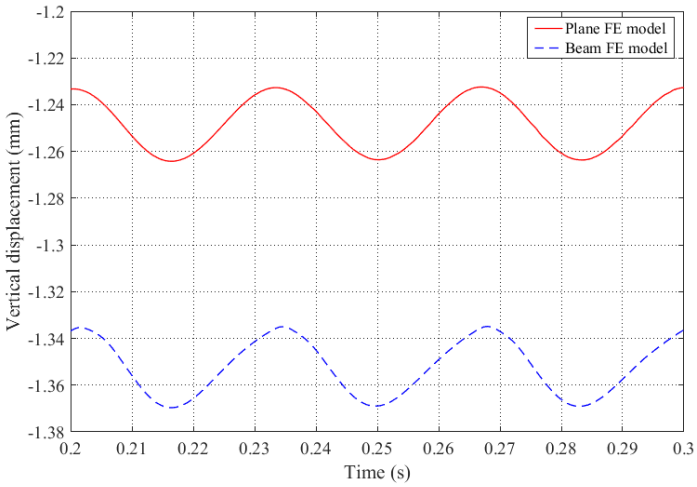

Fig. 23 Vertical displacement at the wheel center with a wheel speed of V = 21 m/s.

The results for (2), a high speed of V= 42 m/s, are plotted in Figs. 24 and 25. Their main features are rather similar to those of (1), a regular wheel speed V= 21 m/s. For example, the trends of the contact forces in both models agree well, local strong oscillations can only be observed in the plane FE model, and the magnitude of the vertical displacement at the wheel center in the beam FE model is larger than that in the plane FE model. Nevertheless, two additional features are noted: first, the amplitude of the contact force increases significantly as the wheel speed increases from V = 21 m/s to V = 42 m/s; second, the pinned-pinned resonance is not excited in either model at the high wheel speed.

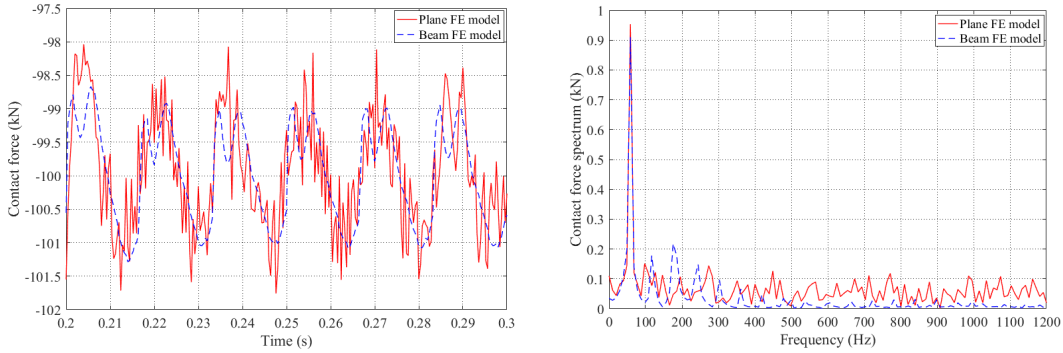

(a) (b)

Fig. 24 Contact force for rail/wheel vibration with a wheel speed of V = 42 m/s: (a) time-history of the contact force; (b) the contact force spectrum.

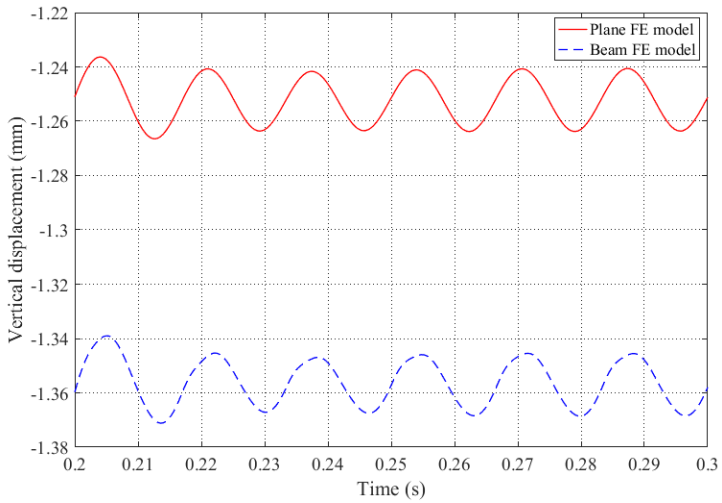

Fig. 25 Vertical displacement at the wheel center with a wheel speed of V = 42 m/s.

4.3 Rail-Wheel Vibration Subjected to Two Rolling Wheels

To investigate the interaction effect of multiple wheels on the rail, a vehicle consisting of two wheels is considered. As shown in Fig. 26, the two wheels are connected to a bogie frame through two primary suspensions, and the bogie frame is further connected by a secondary suspension to the vehicle body, which is approximated as a sprung mass and a dead force. The CW-200 bogie frame,[53] widely used in Mainland China and Hong Kong, is selected here and modeled as a TB with a circular cross-section whose dimension is derived using the Rayleigh's method according to the natural frequency. The secondary suspension is modeled as a linear spring element and a dashpot element. The parameters of both the bogie frame and the secondary suspension are derived according to Ref. 45 and summarized in Table 5.

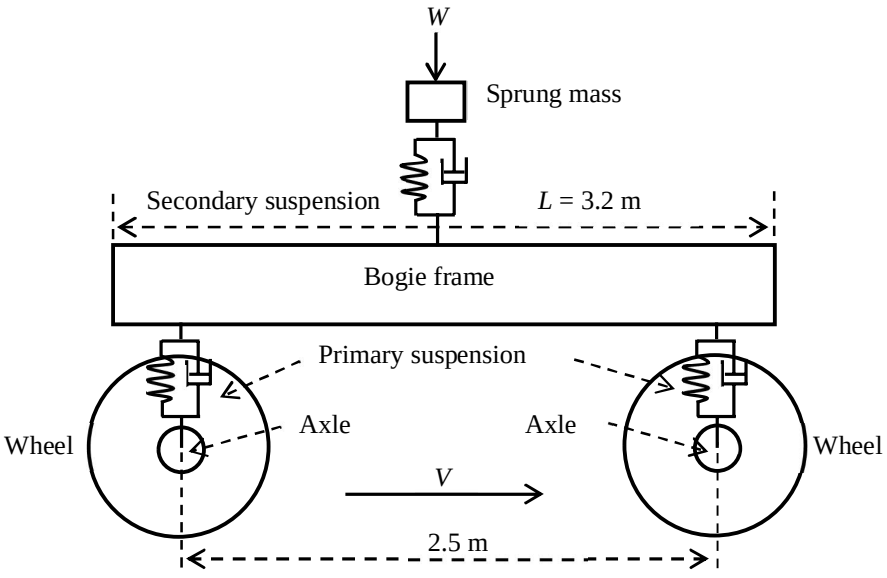

Fig. 26 Vehicle structure including the bogie frame and the secondary suspension.

Table 5. Parameters of the bogie frame and the secondary suspension.

Components	Parameters	Values
Secondary suspension	Spring stiffness (kN/m)	350
	Dashpot coefficient (kN·s/m)	80
Bogie frame (CW-200)	Mass m_b (kg)	545
	Frequency of first order bending mode (Hz) [54]	56
	Radius of cross-section (m)	0.109
	Length (m)	3.2
	Elastic modulus (GPa)	200
	Poisson's ratio	0.28
	Density (kg/m^3)	4540.4
	Distance between two wheels (m)	2.5

The rail-wheel vibration subjected to two wheels rolling at a regular speed of V= 21 m/s are simulated using the two models, and the results *w.r.t.* the two contact pairs, i.e., the back wheel-rail contact and the front wheel-rail contact, are presented, including the rail-wheel contact force and the vertical displacement at the wheel center during the uniform rolling period, as well as the contact force spectrum transformed from the time domain. Figs. 27 and 28 show the contact forces corresponding to the back and front wheel-rail contact pairs, respectively, while Fig. 29 plots the vertical displacements at the back and front wheel centers. Most observations on the vibrational behaviors of both the back and front wheel-rail contact pairs are quite similar to those of the single wheel-rail contact pair shown in Figs. 22 and 23, which indicates that the time-averaged loads are uniformly distributed to the front and back wheels to a certain extent. Thus, using a single rolling wheel in simulation is reasonable for general cases. Nonetheless, severer vibration is noted when two wheels instead of one single wheel are considered on the rail. For example, the amplitude of the contact force for two wheels is larger than that for one single wheel, see Figs. 22 and 27. Additionally, the principal frequencies, the trends of the contact forces and the vertical displacements at the wheel centers obtained from both models are consistent, while strong oscillations at high frequencies can only be observed in the plane FE model, which is similar to the case of a single rolling wheel.

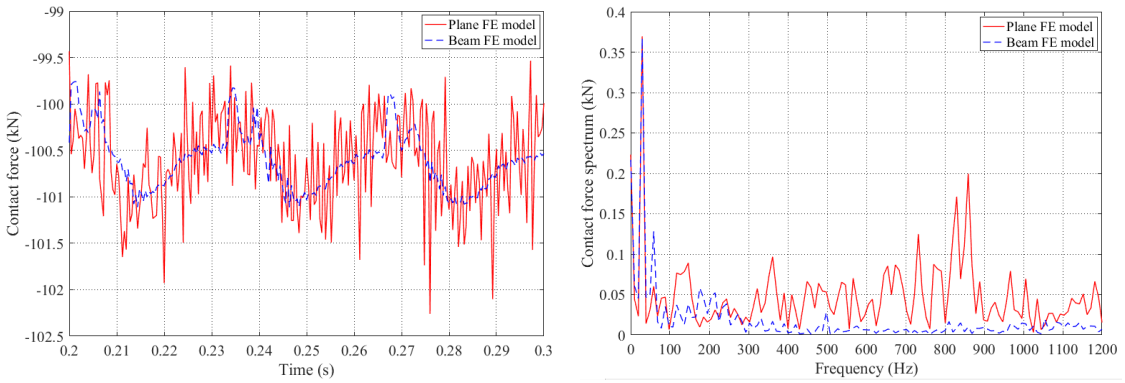

(a) (b)

Fig. 27 Contact force for the back wheel-rail interaction: (a) time-history of the contact force; and (b) the contact force spectrum.

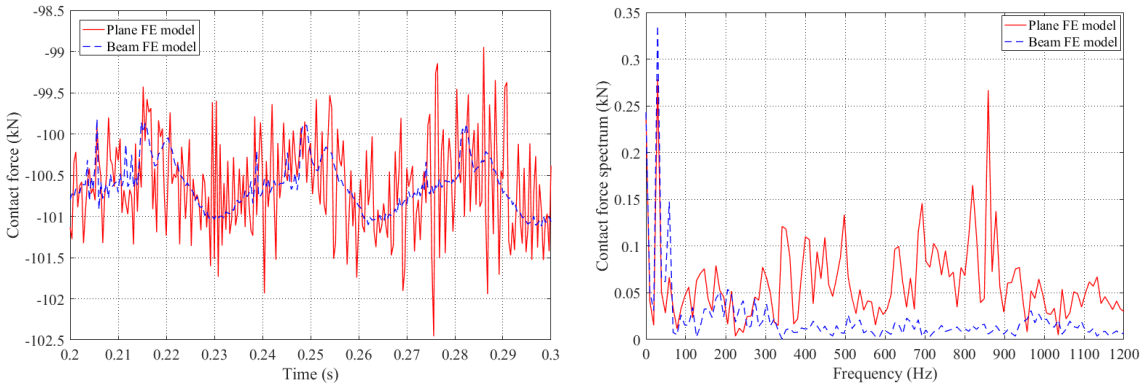

(a) (b)

Fig. 28 Contact force for the front wheel-rail interaction: (a) time-history of the contact force; and (b) the contact force spectrum.

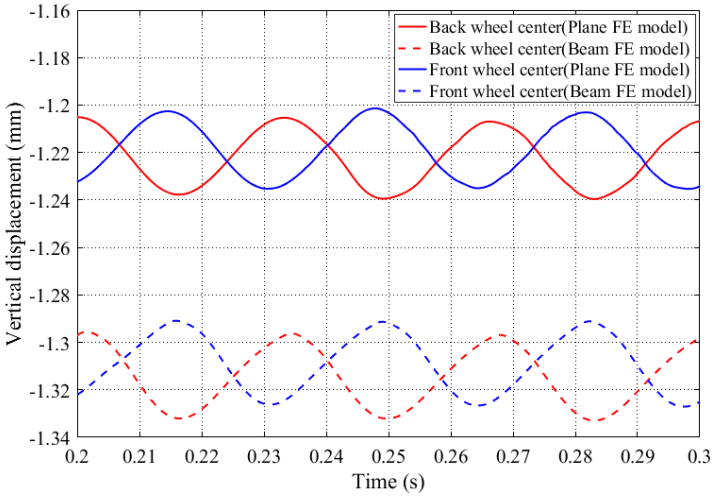

Fig. 29 Vertical displacement at the back and front wheel centers.

4.4 Discussion

From the above simulations it can be seen that both the beam FE model and the plane FE model can predict certain fundamental features of the rail-wheel vibration, e.g., the resonances corresponding to the sleeper-passing frequency, and the trends of the contact force and displacement. Nevertheless, the plane FE model shows superiorities over the beam model, at least in the following aspects: first, the vibrational behaviors of the rail corresponding to high frequencies are captured more realistically; second, the contact treatment is more rigorous, in which the contact algorithm is directly applied instead of just the contact spring, which is highly dependent on the Hertzian assumptions; and third, both the wheel and rail are modeled as deformable bodies, thus the stress distribution/concentration can be readily considered, which, although not discussed here, can be of great significance for the fatigue and failure analysis.

5. Conclusion

In this paper, two numerical models, i.e., the beam FE model and the plane continuum FE model, which are widely applied in simulating rail-wheel vibration, are developed and compared. The beam FE model is developed based on Wu and Thompson's work, where the rail is modeled by TB elements and the rail-wheel contact is approximated by a Hertzian spring. In the plane FE model, both the wheel and rail are modeled using Q4 elements, and the rail-wheel contact is treated using the direct contact algorithm. The beam FE model is generally more time-saving than the plane FE model, although techniques such as the transition mesh scheme introduced in the latter can considerably improve the efficiency. Examples of rail-wheel interactions are used to compare the two models. It is found that certain features and trends of the simulated results obtained from both models are rather similar; e.g., the principal frequencies of the contact force and the vertical displacement at the wheel center are just the corresponding sleeper-passing frequencies. Nevertheless, it is impressive that the plane FE model has superiorities, especially for analyzing the rail-wheel vibration at high frequencies. As the contact force is usually expected to have a strong influence on the rail corrugation, it is often the first concern of engineers, and so detailed discussions regarding it have been presented in this paper. The contact force predicted by the beam FE model is a rather smooth function of time and is different from, for instance, the rail acceleration, which contains a considerable amount of high frequency content. Although only two typical numerical models are analyzed in this paper, the obtained features are universal for the two model categories, i.e., the beam and the plane continuum FE models. Thus, the present study can be of considerable help for designers and engineers in the railway industry in achieving a trade-off between the simulation demands and the computational cost.

It is worth mentioning that the comparison of the beam model and continuum model in the present study is mainly focused on a 2D case that considers the vertical vibration, which is usually the most important dynamic mode in the rail-wheel system. Nevertheless, it can be naturally extended to a 3D case by applying a 3D beam or continuum models to consider both the vertical and lateral vibrations, which are also important in some cases, e.g., a vehicle running on a curved track. Additionally, since explicit time integration is adopted to simulate the mechanical process of the rail-wheel interaction without an iteration involved, the main challenge for 3D simulations is still the computational cost according to the current computational power.

Acknowledgment

The authors acknowledge the support of the Natural Science Foundation of China (11802107), the Natural Science Fund in Shaanxi Province (2018JQ5031), the Jiangsu Science Fund for Youth (BK20150479), the Natural Science Fund for Colleges and Universities in Jiangsu Province (15KJB130002) and the support of the Entrepreneurship and Innovation Doctor Program in Jiangsu Province.

References

1. L. Ling, J. Han, X. Xiao and X. Jin, Dynamic behavior of an embedded rail track coupled with a tram vehicle, *Journal of Vibration and Control,* **23**(14) (2017) 2355-72.
2. S. K. Sharma and A. Kumar, Dynamics analysis of wheel rail contact using FEA, *Procedia Engineering,* **144** (2016) 1119-28.
3. G. Yue, Z. Xu, L. Wang, C. Liu and T. Ren, WSN-based vibration characteristic research for various railway track structures for pattern classification, *International Journal of Pattern Recognition and Artificial Intelligence,* **30**(10) (2016) 1-2.
4. D. Nguyen, K. Kim and P. Warnitchai, Simulation procedure for vehicle-substructure dynamic interactions and wheel movements using linearized wheel-rail interfaces, *Finite Elements in Analysis and Design,* **45**(5) (2009) 341-56.
5. P. J. Remington, Wheel/rail noise—Part I: Characterization of the wheel/rail dynamic system, *Journal of Sound and Vibration,* **46**(3) (1976) 359-79.
6. M. Munjal and M. Heckl, Vibrations of a periodic rail-sleeper system excited by an oscillating stationary transverse force, *Journal of Sound and Vibration,* **81**(4) (1982) 491-500.
7. S. Grassie, R. Gregory, D. Harrison and K. Johnson, The dynamic response of railway track to high frequency vertical excitation, *Journal of Mechanical Engineering Science,* **24**(2) (1982) 77-90.
8. Y. S. Wu, Y. B. Yang and J. D. Yau, Three-Dimensional Analysis of Train-Rail-Bridge Interaction Problems, *Vehicle System Dynamics,* **36**(1) (2001) 1-35.
9. Y. B. Yang and Y. S. Wu, A versatile element for analyzing vehicle–bridge interaction response, *Engineering Structures,* **23**(5) (2001) 452-69.
10. Y. S. Wu and Y. B. Yang, Steady-state response and riding comfort of trains moving over a series of simply supported bridges, *Engineering Structures,* **25**(2) (2003) 251-65.
11. N. Meysam, S. Morad and M. Mohammad, Vibration Analysis of Railway Tracks Considering Weld Surface Irregularities, *International Journal of Structural Stability and Dynamics,* **16**(06) (2016) 1550024.
12. M. T. Tran, K. K. Ang and V. H. Luong, Multiple-Railcar High-Speed Train Subject to Braking, *International Journal of Structural Stability and Dynamics,* **17**(07) (2017) 1750071.
13. R. Clark, P. Dean, J. Elkins and S. Newton, An investigation into the dynamic effects of railway vehicles running on corrugated rails, *Journal of Mechanical Engineering Science,* **24**(2) (1982) 65-76.
14. H. Ilias, The influence of railpad stiffness on wheelset/track interaction and corrugation growth, *Journal of Sound and Vibration,* **227**(5) (1999) 935-48.
15. A. Hosseinkhani and D. Younesian, Vibro-Acoustic Analysis of the Railway Tracks with Fractional Railpads and Nonlinear Ballast, *International Journal of Structural Stability & Dynamics,* **17**(9) (2017) 1750105.

16. T. X. Wu and D. Thompson, Analysis of lateral vibration behavior of railway track at high frequencies using a continuously supported multiple beam model, *The Journal of the Acoustical Society of America,* **106** (1999) 1369-76.
17. T. X. Wu and D. Thompson, A double Timoshenko beam model for vertical vibration analysis of railway track at high frequencies, *Journal of Sound and Vibration,* **224**(2) (1999) 329-48.
18. T. X. Wu and D. Thompson, Vibration analysis of railway track with multiple wheels on the rail, *Journal of Sound and Vibration,* **239**(1) (2001) 69-97.
19. T. X. Wu and D. Thompson, A hybrid model for the noise generation due to railway wheel flats, *Journal of Sound and Vibration,* **251**(1) (2002) 115-39.
20. T. X. Wu and D. Thompson, On the impact noise generation due to a wheel passing over rail joints, *Journal of Sound and Vibration,* **267**(3) (2003) 485-96.
21. T. X. Wu, Parametric excitation of wheel/track system and its effects on rail corrugation, *Wear,* **265**(9) (2008) 1176-82.
22. S. Kaewunruen, T. Lewandrowski and K. Chamniprasart, Dynamic Responses of Interspersed Railway Tracks to Moving Train Loads, *International Journal of Structural Stability and Dynamics,* **18**(01) (2018) 1850011.
23. A. Sladkowski and M. Sitarz, Analysis of wheel–rail interaction using FE software, *Wear,* **258**(7) (2005) 1217-23.
24. L. P. Sun, J. Zhang and J. Zhang. Analyses on wheel-rail contact using finite element method during passing through curved track. *International Conference on measuring technology and mechatronics antomation*. IEEE, 2009, p. 728-31.
25. Z. Wen, X. Jin and W. Zhang, Contact-impact stress analysis of rail joint region using the dynamic finite element method, *Wear,* **258**(7) (2005) 1301-9.
26. Y. C. Chen and L. W. Chen, Effects of insulated rail joint on the wheel/rail contact stresses under the condition of partial slip, *Wear,* **260**(11) (2006) 1267-73.
27. E. Kabo and A. Ekberg, Material defects in rolling contact fatigue of railway wheels—the influence of defect size, *Wear,* **258**(7) (2005) 1194-200.
28. S. Bogdański and M. Trajer, A dimensionless multi-size finite element model of a rolling contact fatigue crack, *Wear,* **258**(7) (2005) 1265-72.
29. J. W. Ringsberg, Life prediction of rolling contact fatigue crack initiation, *International Journal of Fatigue,* **23**(7) (2001) 575-86.
30. W. Daves and F. Fischer, Modelling of the plastification near the rough surface of a rail by the wheel–rail contact, *Wear,* **253**(1) (2002) 241-6.
31. C. Chang, C. Wang and Y. Jin, Study on numerical method to predict wheel/rail profile evolution due to wear, *Wear,* **269**(3) (2010) 167-73.
32. G. Chen, Z. Zhou, H. Ouyang, X. Jin, M. Zhu and Q. Liu, A finite element study on rail corrugation based on saturated creep force-induced self-excited vibration of a wheelset–track system, *Journal of Sound and Vibration,* **329**(22) (2010) 4643-55.
33. Z. F. Wen and X. S. Jin, Elastic-Plastic Finite-Element Analysis of Repeated, Two-Dimensional Wheel-Rail Rolling Contact under Time-Dependent Load, *Proceedings of the Institution of Mechanical Engineers, Part C: Journal of Mechanical Engineering Science,* **220**(5) (2006) 603-13.
34. C. Andersson and A. Johansson, Prediction of rail corrugation generated by three-dimensional wheel–rail interaction, *Wear,* **257**(3) (2004) 423-34.
35. M. Naeimi, M. Shadfar and M. Mehrali, Vibration Analysis of Railway Tracks Considering

Weld Surface Irregularities, *International Journal of Structural Stability & Dynamics,* **16**(06) (2016) 1550024.
36. L. Wu, Z. Wen, W. Li and X. Jin, Thermo-elastic–plastic finite element analysis of wheel/rail sliding contact, *Wear,* **271**(1) (2011) 437-43.
37. L. Ramanan, R. Krishna Kumar and R. Sriraman, Thermo-mechanical finite element analysis of a rail wheel, *International Journal of Mechanical Sciences,* **41**(4) (1999) 487-505.
38. M. Petereson, Two-dimensional finite element simulation of the thermal problem at railway block braking, *Proceedings of the Institution of Mechanical Engineers, Part C: Journal of Mechanical Engineering Science,* **216**(3) (2002) 259-73.
39. C. Sun, J. Zhang, C. Wang and X. Zhang. Thermo-contact coupling finite element method analysis of wheel/rail under sliding status. *Information Engineering and Computer Science, 2009* IEEE, 2009, p. 1-4.
40. Y. Zhan, Finite element analysis of vibration excited by rail-wheel interaction, Master's thesis, University of Hong Kong (2014).
41. T. X. Wu and D. Thompson, On the parametric excitation of the wheel/track system, *Journal of Sound and Vibration,* **278**(4) (2004) 725-47.
42. D. Thompson. *Railway noise and vibration: mechanisms, modelling and means of control*. Elsevier Science, 2008.
43. Hong Kong MTR, http://www.mtr.com.hk, 2017.
44. Z. Li, X. Zhao, C. Esveld, R. Dollevoet and M. Molodova, An investigation into the causes of squats—Correlation analysis and numerical modeling, *Wear,* **265**(9) (2008) 1349-55.
45. Q. Li, The CW-200 type bolsterless Bogies (in chinese), *Rolling Stock,* **39**(8) (2001) 6-9.
46. A. Saulot and L. Baillet, Dynamic finite element simulations for understanding wheel-rail contact oscillatory states occurring under sliding conditions, *Journal of Tribology,* **128**(4) (2006) 761-70.
47. S. Iwnicki. *Handbook of railway vehicle dynamics*. CRC press, 2006.
48. *ABAQUS Theory Manual, Version 6.12*. Providence, RI, USA: Dassault Systèmes Simulia Corp. , 2012.
49. P. Wriggers, Computational contact mechanics, *Computational Mechanics,* **49**(6) (2012) 685-.
50. S. H. Lo, D. Wu and K. Y. Sze, Adaptive meshing and analysis using transitional quadrilateral and hexahedral elements, *Finite Elements in Analysis and Design,* **46** (2010) 2-16.
51. Q. Xie, K. Y. Sze and Y. X. Zhou, Drape simulation using solid-shell elements and adaptive mesh subdivision, *Finite Elements in Analysis and Design,* **106** (2015) 85-102.
52. Q. Xie, K. Y. Sze and Y. X. Zhou, Modified and Trefftz unsymmetric finite element models, *International Journal of Mechanics and Materials in Design,* **12**(1) (2016) 53-70.
53. Changchun Railway Vehicles Co. LTD, http://www.cccar.com.cn/, 2017.
54. Z. S. Ren, S. G. Sun and Z. M. Liu, Dynamic simulation of the passenger cars with elastic bogies, *Journal of the China Railway Society,* **26**(4) (2004) 31-5.